

Single-process 3D-Printed Triaxial Accelerometer

Matic Arh Janko Slavič*

Cite as:

Arh M, Slavič J: Single-Process 3D-Printed Triaxial Accelerometer. *Advanced Materials Technologies*, 2022, <https://doi.org/10.1002/admt.202101321>

Prof. dr. Janko Slavič

University of Ljubljana

Faculty of Mechanical Engineering

Aškerčeva cesta 6

1000 Ljubljana, Slovenia EU

Email Address: janko.slavic@fs.uni-lj.si

Keywords: *accelerometer, 3D printing, piezoresistivity, functional filaments, fused filament fabrication, thermoplastic material extrusion*

For thermoplastic material extrusion 3D-printing functional filaments with electrically conductive, piezoresistive, piezoelectric, capacitive or magnetic properties were developed. The functional filaments resulted in piezoresistive static/quasi-static sensors; however, these 3D-printed sensors were manufactured in several processes, *e.g.*, the creation of highly conductive paths using embedded copper wires or by silver inking. The multi-process 3D printing of sensors presents an obstacle to smart functional 3D-printed structures where the sensory element is *in-situ* printed at the location and orientation of use, including the electrical paths.

This research introduces a three axial piezoresistive accelerometer where the whole sensor, including highly conductive electrical paths, is printed in the same process of thermoplastic material extrusion. The structural components of the sensor are printed with a non-conductive polylactide material, the sensory element with a conductive material that has a relatively high resistivity, and the electrical paths with a conductive material that has a relatively low resistivity. As discussed in the manuscript with single-process sensors, the functional tuning of sensors is as easy as changing the design.

The design and manufacturing solutions researched for the triaxial accelerometer can be applied to other 3D-printed sensors, *e.g.*, force sensors and opens up the possibility of a single-process 3D-printed smart structure.

1 Introduction

Advances in materials science enabled the application of additive manufacturing technology also known as 3D printing, for manufacturing of electronic devices [1]: *e.g.* inkjet printing technology [2, 3], direct ink writing [4], screen printing [5], aerosol jet printing [6], and thermoplastic material extrusion (TME) [7].

This manuscript focuses into TME as it is currently the most widely applied 3D-printing technology [8, 9] in the field of non-electronic devices. Due to its ease of use and low cost it is especially appropriate for prototyping; however, recent progress has made it possible to use TME as a manufacturing technology for innovative and feasible smart structures [10], actuators [11], sensors [12, 13], batteries [14] and metamaterials [15].

3D-printing showed great potential for strain sensing based on the piezoresistive effect [12, 16, 17]. Since piezoresistivity denotes strain-dependent electrical resistivity [18, 19], the structure has to be electrically conductive to exhibit a piezoresistive effect. The thermoplastic filaments that are normally used for TME are, however, electrically non-conductive. By incorporating electrically conductive particles *e.g.*, carbon black (CB) [7], carbon nanotubes (CNT) [20], multiwalled carbon nanotubes (MWCNT) [21, 22], silver [23, 24], copper [24], or a nickel and tin alloy [25], into a non-conductive, thermoplastic matrix, electrical conductivity can be achieved. The volume ratio of the conductive filler has to exceed the percolation threshold when the conductive fillers form conductive networks inside the insulating matrix [26] and thus conduct an electrical current. When a mechanical load is applied to such a composite, conductive networks rearrange and the electrical resistivity changes [27], which is the main mechanism of piezoresistivity in TME structures.

On one hand, the conductive composites for TME conductive filaments have to be optimised to achieve a satisfactory printability and conductivity [28]. On the other hand, TME process parameters have a great influence on the material properties of the 3D-printed structure and can differ from the material properties of the filament [29]. The conductive behaviour of the 3D-printed structure is therefore difficult to predict, due to the nonlinear influence of the process parameters [29], the process parameter's interactions [30] and the anisotropy [31]. Furthermore, poor electrical contacts can cause a high contact resistance [30], which results in signal distortion. To predict the conductive behaviour of TME structures the finite-element method (FEM) [31] and the lumped-element models [32, 33] can be applied.

The development of electrically conductive filaments led to prototype piezoresistive sensors, see Leight *et al.*, [34] where a silver-coated epoxy was used in a separate process to maintain the ohmic contact during the testing. Typically, the 3D-printed sensors are manufactured in two processes: in the first process, the sensory element and the structural support are 3D printed, and in the second process wiring or other processes are completed. This two-process approach can be observed in Christ *et al.* for a unidirectional [21]/bidirectional [35] strain sensor, in Stano *et al.* for a load cell [36], in Kim *et al.* for a multi-axial force sensor [37], in Gooding and Fields for an embedded strain sensor [38], in Al-Rubaiai *et al.* for

a wind sensor [39], in Hohimer *et al.*, Georgopoulou *et al* for a soft pneumatic actuator with an embedded strain sensor [40, 41] and in Watschke *et al.* for a geometrically inovative strain sensor [42]. For details about wiring to the outside system by soldering/heating wires directly into the thermoplastic material, see [35, 36, 38]; for applying adhesives (copper tape, epoxy adhesive), see [42–44]. Already, Leigh *et al.* [34] discussed single-process approaches where a 3D printed banana socket was discussed for applications with low dynamic loads. For high dynamic loads, painting a connection with silver paint [45, 46] to reduce the contact resistance [30] is very desirable. Additional processes can include the creation of highly conductive paths using embedded copper wires [47] or silver paint [48] and removing support material [37, 48].

A single process is especially difficult to achieve in multi-axial dynamic sensors, *e.g.*, an accelerometer, where inertial effects and motion of the connectors significantly impact on the sensor’s performance. Due to the multi-axial sensing, the need for supports and highly conductive paths is also difficult to avoid. In the manuscript the design of a 3D-printed triaxial accelerometer that can be manufactured in a single process is presented. The presented accelerometer is manufactured and experimentally measured. The presented single-process approach is easily modified and integrated into the device’s structure at the location needed and with the orientation required.

2 Results and Discussion

2.1 Single-process multi-functional material accelerometer design and manufacturing process

The design of the accelerometer printed in a single-process is shown in **Figure 1** (a). Three different functional thermoplastic materials are used: electrically insulating material for the support structure (PLA by Plastika Trček), piezoresistive and conductive thermoplastic material (PLA/CB by Protopasta) for the sensory element and the highly electrically conductive material (PLA/copper by Electrifi) for the electrical connectivity, Figure 1 (c). Each filament was printed with a seperate printing tool using the customized Motion System and ToolChanger from E3D [49]. As a result, no excess material (*e.g.*, wipe tower) and manual intervention were necessary. Figure 1 (a) shows the measurement coordinate system, the sensing elements and the inertia-excited beams (*e.g.*, beam X is in bending load if excited in the coordinate axis x).

The accelerometer follows the single-axis design principles [48]: the piezoresistive sensing elements have

to be located at the strain concentrations, the strain sensitivity for the excited axis should be high, the cross-axis excitation should be small, and the conductive paths should be significantly more conductive than the conductivity in the sensing elements.

A high axial and low cross-axis sensitivity are achieved with perpendicular positioning of the beams X, Y and Z; furthermore the width/height ratio should be large, see Figure S1, resulting in a relatively low natural frequency in the measurement direction, while the other two directions have high natural frequencies. The strain conditions were verified with a FEM harmonic analysis in the subresonance region, see Figure 1 (b). Simulations confirmed that strain concentrations appear in the beam perpendicular to the applied acceleration. The location of the strain concentrations is at the surface of the beam in the vicinity of the sensory element.

The difference in the conductivity of the sensing element and the conductive paths was achieved by using functional materials with significant differences in resistivity: the PLA/copper resistivity is $0.006 \Omega \text{ cm}$ while the PLA/CB resistivity is $15 \Omega \text{ cm}$. Additionally, the resistivity is proportional to the length and inversely proportional to the cross-section. Consequently, the conductive paths are short and with a high cross-section, and vice-versa for the sensing element, Figure 1 (c). The center hole of the accelerometer is used to fix the accelerometer to the PCB plate, Figure 1 (a). The triaxial sensor system is electrically connected to the data-acquisition system through the connecting pins V_{GND} , V_x , V_y and V_z , Figure 1 (a) bottom view, Figure S3. Wiring of the sensing elements through the conductive paths to pins V_{GND} (common ground), V_x (sensing element x), V_y (sensing element y) and V_z (sensing element z) is presented in Figure 1 (c). In addition to measuring the voltage drop (u_x , u_y , u_z), the current through sensing elements i_x , i_y , i_z is measured. The quotient between the measured voltage and the current is, via Ohm's law [50], proportional to the sensing element's resistance: $R_x(t)$, $R_y(t)$, $R_z(t)$. During acceleration, the mechanical loads to the sensory elements result in a change of resistivity (due to the piezoresistivity phenomena); this change in resistivity will later be related to the excitation acceleration.

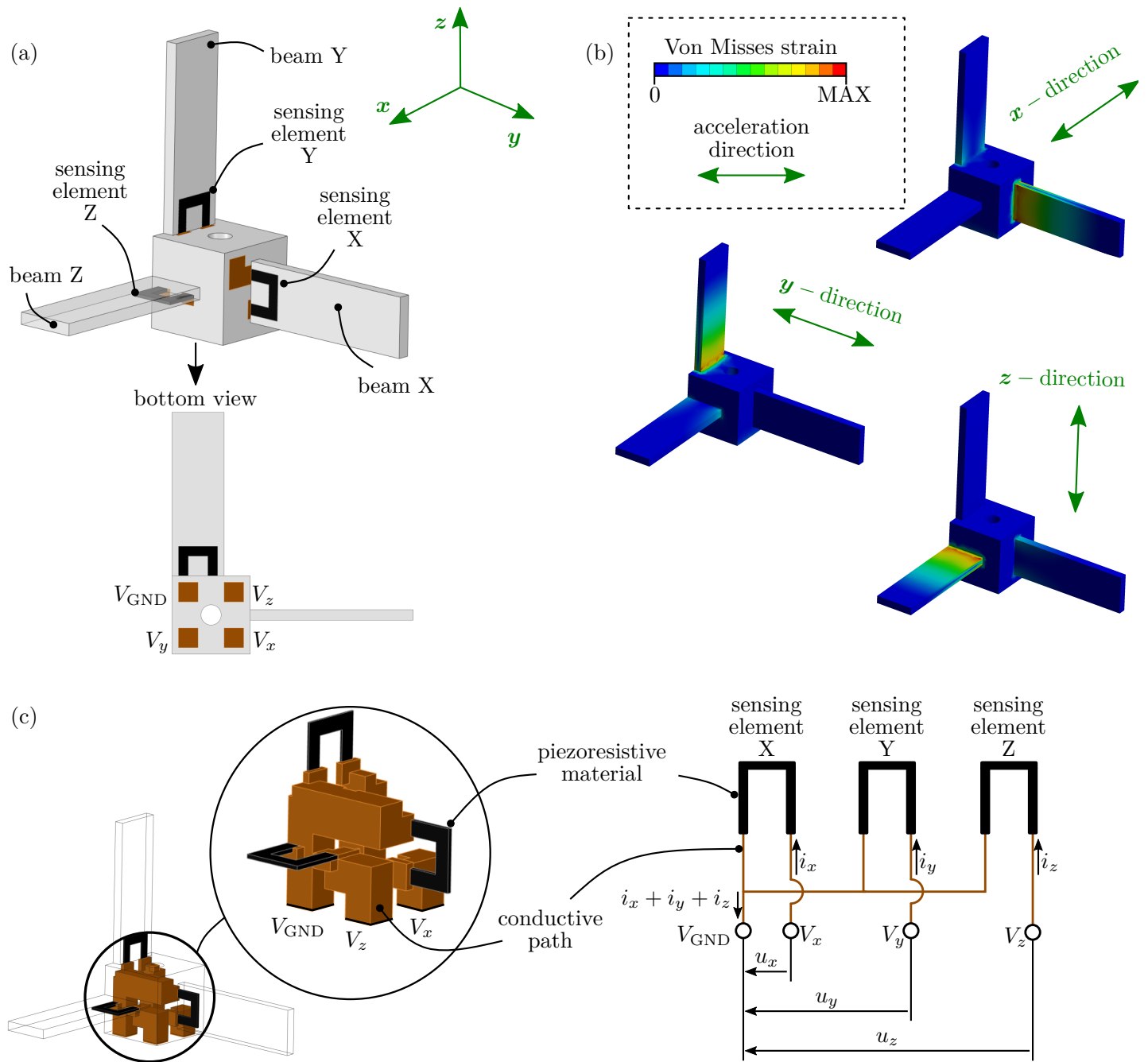


Figure 1: (a) Accelerometer's design, (b) Von Mises strain from FEM harmonic analysis in subresonance, (c) embedded sensory system with wiring diagram

2.2 Accelerometer's characteristics

The characteristics of the 3D-printed accelerometer were experimentally measured as shown in **Figure 2**. The 3D-printed accelerometer was mounted on the electrodynamic shaker and harmonically excited with a constant-amplitude excitation acceleration $a_{exc=i}(t)$, where i represents one of the x , y , z excitation directions. For each excitation direction, the 3D-printed accelerometer was positioned with two beams perpendicular to the excitation direction. Figure 2 (b) shows the setup for the x axis where the beams X

and Y are excited in the bending mode; however, as seen in Figure 1 (b), the mechanical stress at the location of the sensor element is significantly higher in the X beam and very small in the Y and Z beams. If the excitation direction was in y or z direction, the beams Y or Z would be exposed to the most mechanical stress, respectively.

Due to the piezoresistivity, the changes in mechanical stress are measured as changes in the resistivity. Figure 2 (c) shows the measured resistance of the sensor elements x , y and z during excitation in the X direction with an amplitude of $a_{\text{exc}=x}(t) = 50 \text{ m/s}^2$ at frequency of 400 Hz. Next to the 3D-printed accelerometer, a classic piezoelectric triaxial accelerometer was placed for a reference measurement. In Figure 2 (a) the read-out from the classic accelerometer is shown: $a_x(t)$, $a_y(t)$, $a_z(t)$. Since x is the controlled axis, an amplitude of 50 m/s^2 at 400 Hz is measured. The measured accelerations in the transverse direction $a_y(t)$, $a_z(t)$ are at least one order of magnitude smaller and are the result of the dynamic properties of the system, the cross-axis sensitivity, and the noise.

The measured resistance in the sensor elements $R_x(t)$, $R_y(t)$, $R_z(t)$ is shown in Figure 2 (c); for clarity the mean values are subtracted. The change in resistance in the excitation direction is significantly higher when compared to the transverse directions; however, significantly more noise is present than in the classic piezoelectric sensor. The more dominant effect of noise in case of prototype accelerometer can be attributed to the lower resolution of analog to digital conversion, namely 16 bits for prototype accelerometer and 24 bits for commercial accelerometer. To additionally reduce effect of noise, more complex conditioning circuits could be applied.

Figure 2 shows the axial and cross-axial time-domain performance during excitation in the x direction, and similar results were obtained for y and z directions.

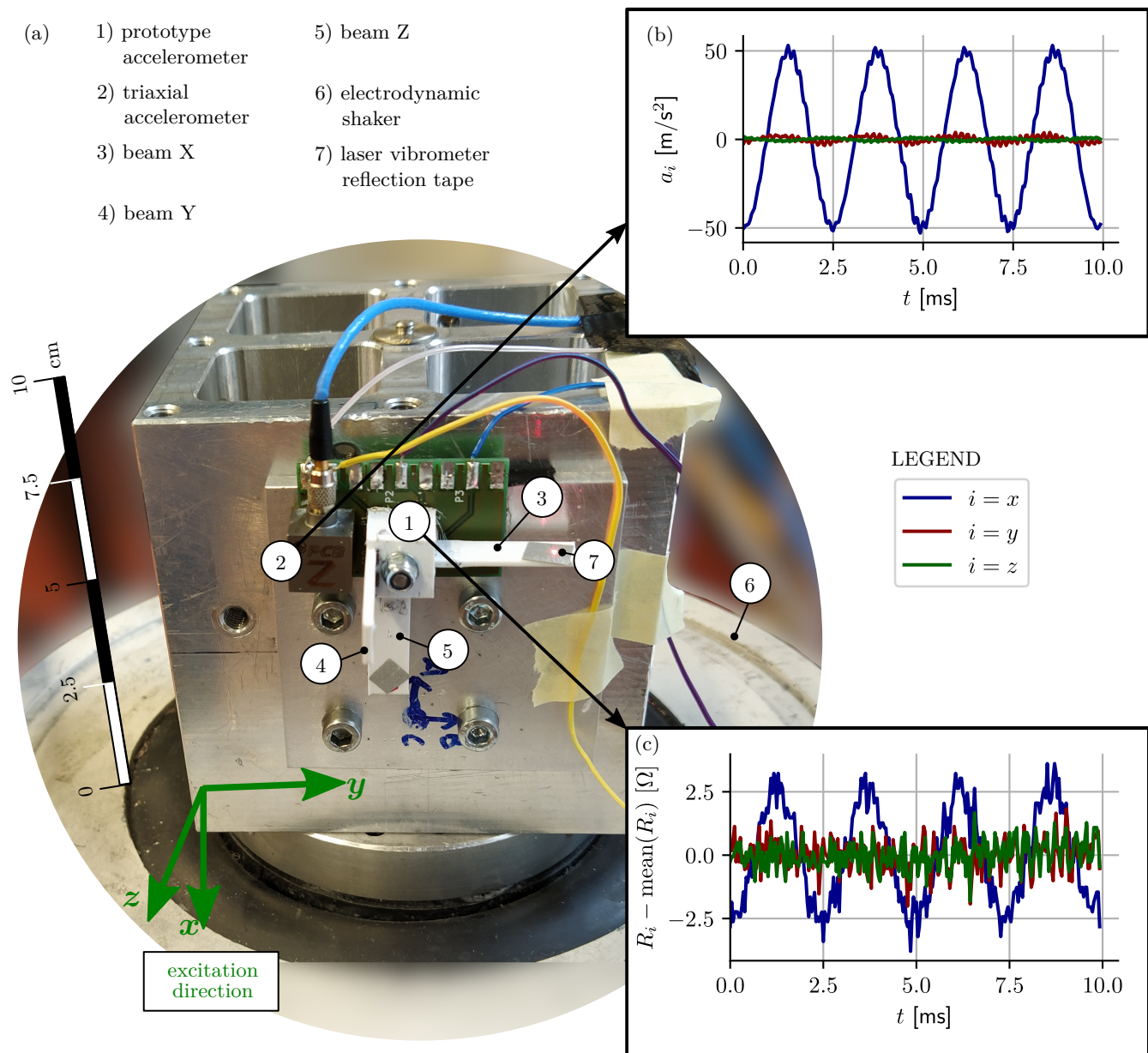


Figure 2: (a) base acceleration in x direction (50 m/s² amplitude at 400 Hz) (b) time-domain results of conventional accelerometer, (c) time-domain results of 3D-printed accelerometer.

To evaluate the frequency-dependent behaviour of the 3D-printed accelerometer, a constant-amplitude sine-sweep (5 octave/min) excitation from 20 to 1000 Hz was performed. The conventional and 3D-printed accelerometers were rotated to achieve acceleration in three perpendicular directions x , y , z . Sine-sweeps were performed at an amplitude of 10 m/s², 30 m/s² and 50 m/s². The measured time-domain signals were transformed to the frequency-domain $R_i(t) \rightarrow \tilde{R}_i(f)$, $a_i(t) \rightarrow \tilde{a}_i(f)$ and averaged over 6 sine-sweeps. $\tilde{R}_i(f)$ and $\tilde{a}_i(f)$ denote the amplitudes of the resistance of the sensing element and the base acceleration (both are complex values) where i corresponds to the coordinate system axes x , y , z . The ratio $\tilde{S}_{ij}(f)$ de-

finds the sensitivity of the piezoresistive element in the i direction when excited in the j direction:

$$\tilde{S}_{ij}(f) = \frac{\tilde{R}_i(f)}{\tilde{a}_{\text{exc}=j}(f)}, \quad i, j = x, y, z \quad (1)$$

When $i = j$, the axial sensitivity and $i \neq j$ the cross-axis sensitivity is measured.

In **Figure 3** (a), (b), and (c) the axial and the cross-axis sensitivities of the sensing elements X, Y and Z at the excitation amplitude of 50 m/s^2 are shown. In Figure 3 (d) the sensitivity at excitation amplitudes of 10 m/s^2 , 30 m/s^2 and 50 m/s^2 are shown. From the results it is clear that the cross-axis sensitivity is significantly smaller than the axial (8% highest value, most measurements below 3%, see Figure S9, S10, S11). Furthermore, it is clear that for the tested excitation range, the sensitivity at a particular frequency is constant (a slight deviation was observed in the natural frequency of the element X). Furthermore, in the frequency range significantly below the first natural frequency, the sensitivity can be considered constant; this region is usually considered the usable frequency range of the inertial mass accelerometer, (*e.g.*, $0.3 f_{0i}$ [51]). The average sensitivities in the usable frequency range (20-150 Hz) are $\tilde{S}_{xx} \approx 17.5 \text{ m}\Omega \text{ s}^2/\text{m}$, $\tilde{S}_{yy} \approx 12.6 \text{ m}\Omega \text{ s}^2/\text{m}$, $\tilde{S}_{zz} \approx 2.5 \text{ m}\Omega \text{ s}^2/\text{m}$. In the range significantly below the natural frequency the phase is also close to zero, Figure 3 (e).

In Figure 3 the natural frequencies are marked with vertical dashed lines: $f_{0x} \approx 484 \text{ Hz}$, $f_{0y} \approx 561 \text{ Hz}$ and $f_{0z} \approx 678 \text{ Hz}$. In general, lower natural frequencies result in a higher sensitivity [48]; this is also clear from Figure 3 (d) where the sensing element Z has the highest natural frequency and the smallest sensitivity (at an excitation level of 10 m/s^2 already well contaminated with noise). See also Figures S4, S5, S6.

The 150 Hz frequency range and the amplitude range of at least 50 m/s^2 and below 8% of cross-axis sensitivity characteristics of prototype accelerometer are comparable to the performance of commercially accessible MEMS accelerometers [52, 53].

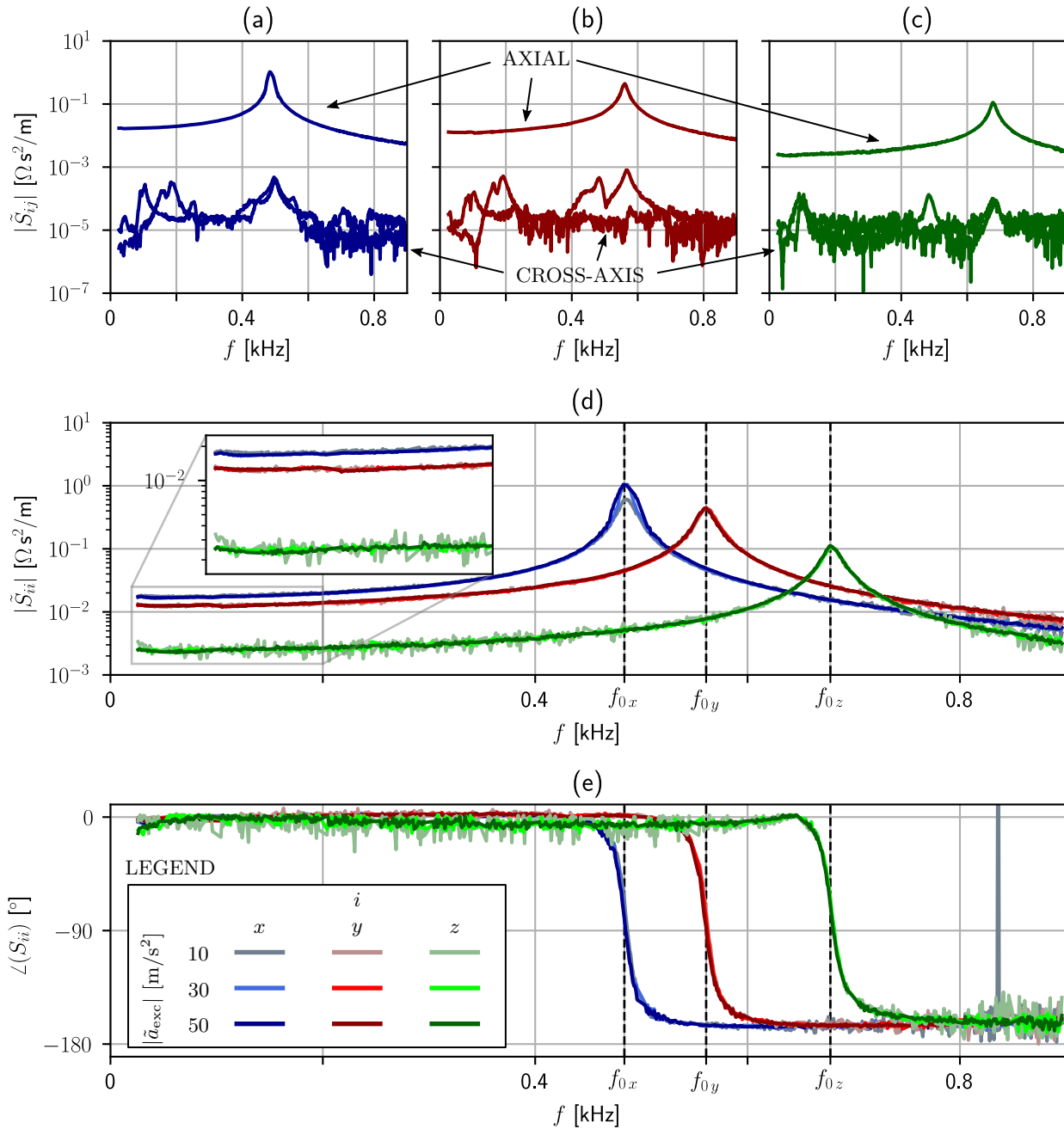


Figure 3: Axial and cross-axis sensitivity at 50 m/s^2 : (a) sensing element X, (b) sensing element Y, (c) sensing element Z. (d) Amplitude of axial sensitivity for sensing elements X, Y and Z at excitation amplitudes of 10 m/s^2 , 30 m/s^2 and 50 m/s^2 e) Phase of axial sensitivity for sensing elements X, Y and Z at excitation amplitudes of 10 m/s^2 , 30 m/s^2 and 50 m/s^2 .

2.3 Modifying accelerometer's behaviour

The sensitivity of the single-process 3D-printed accelerometer is easily changed by changing the design and sending it again to the 3D printer; this task will be discussed next. The design discussed in Section 2.2 has the first three natural frequencies in the range from 484 Hz to 678 Hz and consequently the beam with the lowest natural frequency has the highest sensitivity (and vice-versa). The sensitivity is

proportional to the mechanical behaviour of the beam, see Figure 3 (a), (b), (c) and the Euler-Bernoulli beam model can be used to estimate the sensing behaviour [48], where the first natural frequency of the fixed-free beam is defined as [54]:

$$f_0 = \frac{3.516}{2\pi} \sqrt{\frac{EI}{\rho A L^4}}. \quad (2)$$

E represents the Young's modulus, I the second moment of area, ρ the density, A the cross-section and L the length of the beam. The differences in natural frequencies of the first design are related to the spread of the equivalent Young's modulus due to the parameters of the 3D-printing process, *e.g.*, build direction. Cross-section A , and length L are the parameters that can be used to tune the natural frequency; here, the length L was used. In the following, it will be shown how to tune the natural frequency of the beam X $f_{0,x}$ to the natural frequency of the beam Y $f_{0,y}$. A similar procedure is used (but not discussed here) for tuning the natural frequency of the beam Z.

In the first step, Equation (2) was rearranged and the equivalent Young's modulus was identified for the beam X:

$$E_x = \left(\frac{2\pi f_{0,x}}{3.516}\right)^2 \frac{\rho A L^4}{I}. \quad (3)$$

The Young's modulus E_x and the goal natural frequency $f_{0,y}$ were used with Equation (2) to obtain the new length L_x :

$$L_x = \sqrt{\frac{3.516}{2\pi f_{0,y}}} \sqrt[4]{\frac{E_x I}{\rho A}}. \quad (4)$$

Initial values for the first design were: $L = 25$ mm, $A = 12.8$ mm², $I = 2.731$ mm⁴ and $\rho = 1250$ kg/m³. The identified equivalent Young's moduli were $E_x = 1.71$ GPa, $E_y = 2.30$ GPa, $E_z = 3.37$ GPa. With the above procedure the new lengths are: $L_x \approx 23$ mm, $L_z \approx 27$ mm. To additionally increase the sensitivity, the width of the sensing element was decreased from 15 mm to 12 mm.

The second design was manufactured and characterized in the same way as the first one, see Sections 2.1 and 2.2, and the resulting natural frequencies were: 531 Hz, 556 Hz and 549 Hz, for X, Y, Z beams, respectively, see also Figure S8. In Table 1 the sensitivities of the 1st and 2nd designs at 30 m/s² excitation amplitude are presented. The sensitivity of the sensing element Y increased by 26 % due to the width change of the sensing element, only. The change in sensitivity of the sensing elements X and Z is at-

tributed to change in the natural frequency and width: 13% decrease in sensitivity for sensing element X and 150% increase for element Z. Similar results are obtained for the excitation amplitudes at 10 m/s² and 50 m/s². The cross-axis sensitivities of the 2nd design are also more than one order of magnitude smaller than the sensitivity (8% highest value most measurements below 3%), see Figures S12, S13, S14.

Table 1: Sensitivities for 1st and 2nd designs at 30 m/s² excitation amplitude

accelerometer	mean sensitivity \pm 2 standard deviation [m Ω / (m/s ²)]*		
	<i>x</i>	<i>y</i>	<i>z</i>
1 st design	17.29 \pm 0.83	12.61 \pm 0.56	2.50 \pm 0.65
2 nd design	15.1 \pm 0.52	15.95 \pm 0.77	6.24 \pm 0.64

* mean and standard deviation of sensitivities in 20-150 Hz are taken into account

3 Conclusion

The design and manufacturing process of a single-process 3D-printed (TME) piezoresistive triaxial accelerometer with no manual intervention is presented. The 3D-printed accelerometer can be printed directly into a smart structure or, as shown here, attached to a PCB using a fixation screw.

The design researched here has 37 \times 37 \times 37 mm³ dimensions and consists of three perpendicular beams attached to the cube. While the size of the prototype accelerometer could be further decreased, the discussed prototype is approx. 1.5-3 times larger in comparison to the commercial accelerometers [53]; however, the fixation surface has similar dimensions - 12x12 mm². Since spatial resolution is limited by fixation surface, the prototype accelerometer can be used in similar scenarios as commercial. Additionally, the mass of the prototype accelerometer is approximately 3 gram which is comparable to the lighter commercial accelerometers which typically range from 0.7 gram to 175 gram [53] and thus minimal mass loading. The accelerometer has a linear response in 10 m/s²-50 m/s² excitation amplitude, low cross-axis sensitivities (8% highest value, most measurements below 3%) and 150 Hz useful frequency range. The sensitivities for the three perpendicular directions are 15 m Ω s²/m, 16 m Ω s²/m and 6 m Ω s²/m. Additionally, the changes in design to tune the accelerometer's performance are discussed.

The presented work shows that TME technology can be used to manufacture triaxial accelerometer with characteristics that are approaching the characteristics of commercially available accelerometers. The accessibility of the TME, possibility of using single technology to manufacture support structure as well as sensing elements and ease of modification can in the future enable the creation of sensors with custom-designed characteristics. The improvement of current characteristics is expected in the future by studying the effects of different process parameters on the electrical resistivity, piezoresistivity and mechan-

ical properties as well as using more sophisticated signal conditioning system and taking further steps towards size reduction.

The single-process 3D printing of sensors is essential for future devices that will be 3D printed in a single-process (sensors as well as the functional and support structure).

4 Experimental Section

Filaments: For printing highly conductive paths the Eletrifi filament [55] from Multi3D was used. Eletrifi is a PLA/Cu composite [56] with a $6 \cdot 10^{-5} \Omega \text{ m}$ volume resistivity. For printing the piezoresistive sensing element, a conductive PLA/CB composite from Protopasta [57] was used. The conductive filament from Protopasta has a resistivity of $0.15 \Omega \text{ m}$ [57]. The non-conductive part of the accelerometer was printed with PLA filament from PLASTIKA TRČEK [58]. All filaments had a 1.75 mm diameter.

Manufacturing process: The accelerometer was 3D printed with in-house-modified Motion System and ToolChanger from E3D [49]. A modified 3D printer enables the simultaneous automatic printing of four filaments with separate extruders. Printing settings for the non-conductive PLA filament [58] for printing non-conductive part of the accelerometer were rectilinear infill pattern, 45° fill angle, 3 external perimeters, 40 mm/s printing speed, 210°C nozzle temperature. Process parameters for the piezoresistive Protopasta filament [57] for printing piezoresistive sensing elements were rectilinear infill, no perimeters, 20 mm/s printing speed, 220°C nozzle temperature. Process parameters for highly conductive Eletrifi [55] for printing highly conductive paths were rectilinear infill pattern, no external parameters, 20 mm/s printing speed, 145°C nozzle temperature. Layer height was 0.2 mm, nozzle diameters 0.4 mm and printing bed was at room temperature (not heated).

Experimental characterization: Mechanical excitation was performed with an LDS V555 electrodynamic shaker. Base accelerations were measured with a PCB 356A32 triaxial IEPE accelerometer. For signal acquisition one NI-9234 and two NI-9215 input modules from National Instruments were used.

Supporting Information

Supporting Information is available from the Wiley Online Library or from the author.

Acknowledgements

The authors acknowledge the partial financial support from the Slovenian Research Agency (research core funding No. P2-0263 and research project No. J2-3045).

References

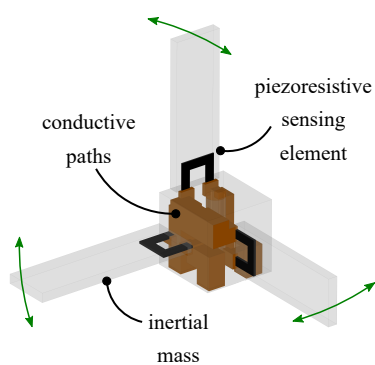
- [1] G. L. Goh, H. Zhang, T. H. Chong, W. Y. Yeong, *Advanced Electronic Materials* **2021**, *7*, 10 2100445.
- [2] P. Jiang, Z. Ji, X. Zhang, Z. Liu, X. Wang, *Progress in Additive Manufacturing* **2018**, *3*, 1 65.
- [3] B. Ando, S. Baglio, *IEEE Instrumentation & Measurement Magazine* **2011**, *14*, 5 36.
- [4] M. Gao, L. Li, Y. Song, *Journal of Materials Chemistry C* **2017**, *5* 2971.
- [5] K. C. Honeychurch, J. P. Hart, *TrAC Trends in Analytical Chemistry* **2003**, *22*, 7 456.
- [6] S. Agarwala, G. L. Goh, W. Y. Yeong, *IEEE Access* **2018**, *6* 63080.
- [7] S. W. Kwok, K. H. H. Goh, Z. D. Tan, S. T. M. Tan, W. W. Tjiu, J. Y. Soh, Z. J. G. Ng, Y. Z. Chan, H. K. Hui, K. E. J. Goh, *Applied Materials Today* **2017**, *9* 167.
- [8] Y. Wang, Y. Zhou, L. Lin, J. Corker, M. Fan, *Composites Part A: Applied Science and Manufacturing* **2020**, *139* 106114.
- [9] M. G. M. Marascio, J. Antons, D. P. Pioletti, P.-E. Bourban, *Advanced Materials Technologies* **2017**, *2*, 11 1700145.
- [10] H. Wu, Y. Tian, H. Luo, H. Zhu, Y. Duan, Y. Huang, *Advanced Materials Technologies* **2020**, *5*, 8 2000093.
- [11] B. A. W. Keong, R. Y. C. Hua, *Advanced Materials Technologies* **2017**, *3*, 2 1700172.
- [12] H. Liu, H. Zhang, W. Han, H. Lin, R. Li, J. Zhu, W. Huang, *Advanced Materials* **2021**, *33*, 8 2004782.
- [13] M. Schouten, G. Wolterink, A. Dijkshoorn, D. Kosmas, S. Stramigioli, G. Krijnen, *IEEE Sensors Journal* **2021**, *21*, 11 12900.
- [14] X. Yu, Y. Liu, H. Pham, S. Sarkar, B. Ludwig, I.-M. Chen, W. Everhart, J. Park, Y. Wang, H. Pan, *Advanced Materials Technologies* **2019**, *4*, 11 1900645.
- [15] S. M. Montgomery, S. Wu, X. Kuang, C. D. Armstrong, C. Zemelka, Q. Ze, R. Zhang, R. Zhao, H. J. Qi, *Advanced Functional Materials* **2020**, *31*, 3 2005319.

- [16] Z. Wang, X. Guan, H. Huang, H. Wang, W. Lin, Z. Peng, *Advanced Functional Materials* **2018**, *29*, 11 1807569.
- [17] W. Zhao, Z. Wang, J. Zhang, X. Wang, Y. Xu, N. Ding, Z. Peng, *Advanced Materials Technologies* **2021**, *6*, 8 2001218.
- [18] G. M. Koo, T. N. Tallman, *Composites Part B: Engineering* **2020**, *190*, December 2019 107907.
- [19] T. D. Gupta, T. Gacoin, A. C. H. Rowe, *Advanced Functional Materials* **2014**, *24*, 28 4522.
- [20] S. Dul, L. Famrbi, A. Pegoretti, *Nanomaterials* **2018**, *8*, 1 49.
- [21] J. F. Christ, N. Aliheidari, A. Ameli, P. Pötschke, *Materials and Design* **2017**, *131* 394.
- [22] A. Dorigato, V. Moretti, S. Dul, S. H. Unterberger, A. Pegoretti, *Synthetic Metals* **2017**, *226* 7.
- [23] Z. Lei, Z. Chen, Y. Zhou, Y. Liu, J. Xu, D. Wang, Y. Shen, W. Feng, Z. Zhang, H. Chen, *Composites Science and Technology* **2019**, *180* 44 .
- [24] M. A. Cruz, S. Ye, M. J. Kim, C. Reyes, F. Yang, P. F. Flowers, B. J. Wiley, *Particle & Particle Systems Characterization* **2018**, *35*, 5 1700385.
- [25] J. C. Tan, H. Y. Low, *Additive Manufacturing* **2018**, *23*, June 294.
- [26] D. D. L. Chung, *Journal of Materials Science* **2020**, *55*, 32 15367.
- [27] F. Avilés, A. I. Oliva-Avilés, M. Cen-Puc, *Advanced Engineering Materials* **2018**, *20*, 7 1701159.
- [28] A. Kalkal, S. Kumar, P. Kumar, R. Pradhan, M. Willander, G. Packirisamy, S. Kumar, B. D. Malhotra, *Additive Manufacturing* **2021**, 102088.
- [29] T. B. Palmić, J. Slavič, M. Boltežar, *Sensors* **2020**, *20*, 16 4542.
- [30] H. Watschke, K. Hilbig, T. Vietor, *Applied Sciences* **2019**, *9*, 4 779.
- [31] J. Zhang, B. Yang, F. Fu, F. You, X. Dong, M. Dai, *Applied Sciences* **2017**, *7*, 1 20.
- [32] A. Dijkshoorn, M. Schouten, G. Wolterink, R. Sanders, S. Stramigioli, G. Krijnen, *IEEE Sensors Journal* **2020**, *20*, 23 14218.
- [33] A. Dijkshoorn, M. Schouten, S. Stramigioli, G. Krijnen, *Sensors* **2021**, *21*, 11 3710.
- [34] S. J. Leigh, R. J. Bradley, C. P. Purcell, D. R. Billson, D. A. Hutchins, *PLOS ONE* **2012**, *7*, 11 e49365.

- [35] J. Christ, N. Aliheidari, P. Pötschke, A. Ameli, *Polymers* **2018**, *11*, 1 11.
- [36] G. Stano, A. Di Nisio, A. Lanzolla, G. Percoco, *Precision Engineering* **2020**, *62* 113 .
- [37] K. Kim, J. Park, J.-h. Suh, M. Kim, Y. Jeong, I. Park, *Sensors and Actuators A: Physical* **2017**, *263* 493.
- [38] J. Gooding, T. Fields, In *58th AIAA/ASCE/AHS/ASC Structures, Structural Dynamics, and Materials Conference*. American Institute of Aeronautics and Astronautics, **2017** URL <https://doi.org/10.2514/6.2017-0350>.
- [39] M. Al-Rubaii, R. Tsuruta, U. Gandhi, C. Wang, X. Tan, *Smart Materials and Structures* **2019**, *28*, 8 084001.
- [40] C. J. Hohimer, G. Petrossian, A. Ameli, C. Mo, P. Pötschke, *Additive Manufacturing* **2020**, *34* 101281.
- [41] A. Georgopoulou, L. Egloff, B. Vanderborght, F. Clemens, *Actuators* **2021**, *10*, 5 102.
- [42] H. Watschke, M. Goutier, J. Heubach, T. Vietor, K. Leichsenring, M. Böl, *Applied Sciences* **2020**, *11*, 1 113.
- [43] M. Arh, J. Slavič, M. Boltežar, *Additive Manufacturing* **2020**, *36* 101493.
- [44] M. Palmieri, J. Slavič, F. Cianetti, *Additive Manufacturing* **2021**, *47* 102303.
- [45] M. Maurizi, J. Slavič, F. Cianetti, M. Jerman, J. Valentinčič, A. Lebar, M. Boltežar, *Sensors* **2019**, *19*, 12 2661.
- [46] M. Maurizi, F. Cianetti, J. Slavič, G. Zucca, M. Palmieri, *Procedia Structural Integrity* **2019**, *24* 390, aIAS 2019 International Conference on Stress Analysis.
- [47] C. Kim, D. Espalin, A. Cuaron, M. A. Perez, M. Lee, E. MacDonald, R. B. Wicker, *Journal of Mechanisms and Robotics* **2015**, *7*, 2.
- [48] M. Arh, J. Slavič, M. Boltežar, *Mechanical Systems and Signal Processing* **2021**, *152* 107475.
- [49] Technical data - motion system and toolchanger, <https://e3d-online.com/pages/toolchanger>, Last accessed 21. July 2021.
- [50] B. Notaros, *Electromagnetics*, Prentice Hall, Upper Saddle River, N.J, **2011**.

- [51] M. Serridge, T. Licht, *Piezoelectric Accelerometers and Vibration Preamplifiers: Theory and Application Handbook*, Brüel & Kjær, **1986**.
- [52] Mems sensors & sensing elements (murata), <https://www.murata.com/~media/webrenewal/support/library/catalog/products/sensor/mems/s47e.ashx>, Last accessed 16. November 2021.
- [53] Technical data - acceleration (kistler), https://www.kistler.com/fileadmin/files/divisions/sensor-technology/test-and-measurement/t-m/_acceleration/900-380a.pdf, Last accessed 16. November 2021.
- [54] S. S. Rao, *Vibration of Continuous Systems*, John Wiley & Sons, Inc., **2006**.
- [55] Technical data - electrifi conductive filament, <http://www.multi3d11c.com>, Last accessed 16. November 2021.
- [56] P. F. Flowers, C. Reyes, S. Ye, M. J. Kim, B. J. Wiley, *Additive Manufacturing* **2017**, *18* 156.
- [57] Technical data - proto-pasta conductive pla, https://cdn.shopify.com/s/files/1/0717/9095/files/TDS__Conductive_PLA_1.0.1.pdf?1771, Last accessed 16. November 2021.
- [58] Technical data - plastika trček pla filament, <https://plastikatrcek.si/en/izdelek/pla-filament>, Last accessed 21. July 2021.

ToC



Based on different functional filaments, three axial piezoresistive accelerometer is 3D printed in a single-process using the thermoplastic material extrusion technology. The single-process design enables a) simple sensitivity tuning and b) *in-situ* printing of smart structures with the sensory element at the location and orientation of use